


Slow-Wave-Based Nanomagnonic Diode

Matias Grassi¹, Moritz Geilen², Damien Louis^{1,2}, Morteza Mohseni², Thomas Brächer², Michel Hehn³, Daniel Stoeffler¹, Matthieu Bailleul^{1,*}, Philipp Pirro², and Yves Henry¹

¹Université de Strasbourg, CNRS, Institut de Physique et Chimie des Matériaux de Strasbourg, UMR 7504, F-67000 Strasbourg, France

²Fachbereich Physik and Landesforschungszentrum OPTIMAS, Technische Universität Kaiserslautern, 67663 Kaiserslautern, Germany

³Institut Jean Lamour, Université de Lorraine, UMR 7198, CNRS, F-54000 Nancy, France

 (Received 17 December 2019; revised 17 July 2020; accepted 17 July 2020; published 18 August 2020)

Spin waves, the collective excitations of the magnetic order parameter, and magnons, the associated quasiparticles, are envisioned as possible data carriers in future wave-based computing architectures. On the road toward spin-wave computing, the development of a diodelike device capable of transmitting spin waves in only one direction, thus allowing controlled signal routing, is an essential step. Here we report on the design and experimental realization of a microstructured magnonic diode in a ferromagnetic bilayer system. Effective unidirectional propagation of spin waves is achieved by taking advantage of nonreciprocities produced by dynamic dipolar interactions in transversally magnetized media, which lack symmetry about their horizontal midplane. More specifically, dipolar-induced nonreciprocities are used to engineer the spin-wave dispersion relation of the bilayer system so that the group velocity is reduced to very low values for one direction of propagation and not for the other, thus producing unidirectional slow spin waves. Brillouin light scattering and propagating-spin-wave spectroscopy are used to demonstrate the diodelike behavior of the device, the composition of which is first optimized through micromagnetic simulations.

DOI: [10.1103/PhysRevApplied.14.024047](https://doi.org/10.1103/PhysRevApplied.14.024047)

I. INTRODUCTION

The isolator, or wave diode, is an essential building block in wave-computing architectures, which is necessary to mitigate unwanted reflections and prevent signal backflow [1]. To act as a diode, that is, to transmit waves in only one direction, and, more generally, to exhibit nonreciprocity, a wave device operated in the linear regime must break time-reversal (T) symmetry [2]. While breaking of T symmetry in photonic and electronic systems requires complex time-dependent externally driven modulations, such as propagating refractive-index perturbation [3] or staggered commutation [4], it happens readily in gyrotropic systems, such as magnetically biased two-dimensional electron gases [5] or plasmas [6], and it exists intrinsically in ferromagnetic and ferrimagnetic materials, which, in a bulk form, constitute the heart of standard microwave isolators [7].

Magnetic materials host spin waves with typical frequencies and wavelengths in the gigahertz-to-terahertz and nanometer-to-micrometer ranges, respectively, which are considered as possible carriers for wave computing or

fast information processing in so-called magnonic circuits [8]. To avoid power losses on signal conversion to the electrical domain, an all-magnon approach [9], where full data processing would be performed within the spin-wave domain, would be highly desirable. In recent years, important steps have been taken in this direction, which include the experimental demonstration of a magnonic majority gate [10] and the design of a magnonic half-adder [11]. Designs of magnonic diodes [12] and unidirectional spin-wave emitters [13] relying on the chiral Dzyaloshinskii-Moriya interaction for producing nonreciprocity have been proposed theoretically but have not been realized yet. Very recently, another type of unidirectional spin-wave emitter was demonstrated experimentally [14], the working principle of which is based on the nonreciprocal magnetodipolar coupling between a nanoscale grating made of hard ferromagnetic nanowires and a magnetically softer thin film. In this scheme, somewhat similar to that of unidirectional surface-plasmon launchers [15], the emitter (the grating) plays an essential role in producing nonreciprocity.

Dipole-induced nonreciprocity is quite ubiquitous in the Damon-Eshbach (DE) or magnetostatic-surface-wave (MSSW) configuration, where the equilibrium magnetization of a thin film lies in the plane and at a right

*matthieu.bailleul@ipcms.unistra.fr

angle to the direction of spin-wave propagation [16]. This configuration is specific in that a dipolar coupling exists between the two (in-plane and out-of-plane) components of the dynamic magnetization [17], which happens to be nonreciprocal. In the presence of top or bottom magnetic asymmetry, this coupling does not average out to zero and translates into counterpropagating surface waves with a given wave number having different frequencies [18–22]. As demonstrated at the millimeter scale with relatively thick films in which symmetry was broken either by addition of a nonmagnetic conductor to one side of the film [23] or by use of a magnetic bilayer stack [24], one can even reach an extreme situation in which, at some frequencies, propagation is possible only in one direction. In the situations described above, the effect can be described simply in terms of localized surface waves, as predicted in the purely dipolar description of DE spin waves. When the film thickness is reduced to the nanometer scale, however, this description becomes incorrect as exchange interaction starts to play a crucial role and spin-wave modes lose their surface character. An adapted strategy to achieve spin-wave unidirectionality then needs to be devised.

In the present work, we proceed further and achieve unidirectional spin-wave propagation in an elementary, translation-invariant, system consisting of an exchange-coupled ferromagnetic bilayer, only several tens of nanometers thick. We engineer the spin-wave dispersion so as to bring the group velocity of spin waves traveling in a particular direction to very low values, while keeping the group velocity of counterpropagating waves large enough to ensure that they travel over long distances. This nonreciprocal slow-wave effect enables us to fabricate a nanomagnonic diode out of a $\text{Co}_{40}\text{Fe}_{40}\text{B}_{20}/\text{Ni}_{80}\text{Fe}_{20}$ bilayer waveguide, which we characterize experimentally using Brillouin light scattering (BLS) and propagating-spin-wave spectroscopy (PSWS) [25]. Two types of numerical simulations are used to support our experimental work. An in-house-developed finite-difference method, which performs a plane-spin-wave normal-mode analysis [26], and which we refer to as “SWIIM,” is used to compute dispersion relations and to optimize the composition of the investigated bilayer system before its fabrication. The program *mumax*³ [27], on the other hand, is used to produce magnetization maps, mostly for illustration purposes. Importantly, an analytical model is first presented as a minimal description of the specific chiral dipolar couplings on which the working principle of the nanomagnonic diode relies.

II. DESIGN PRINCIPLE AND THEORY

A. Design principle

The bilayer system that we consider has a total thickness l of several tens of nanometers. For such a thickness, the two lowest-frequency MSSW branches are close to

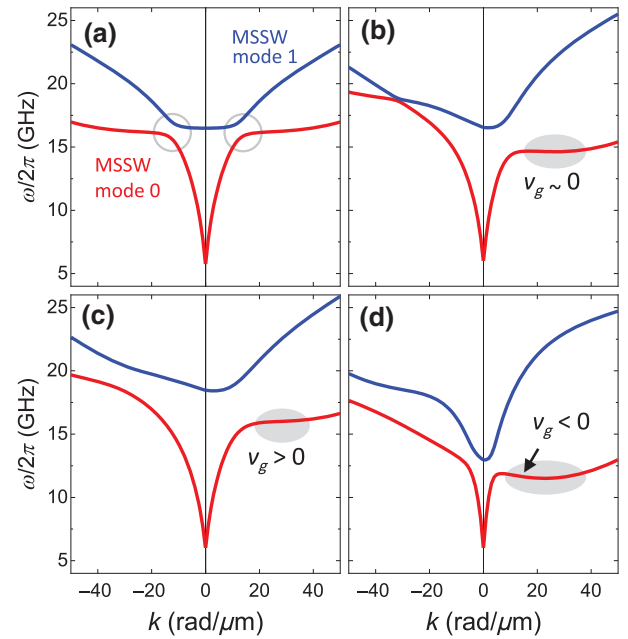


FIG. 1. (a) Dispersion relations for the two lowest-frequency MSSW modes in a 38-nm-thick single layer with an exchange constant of 15 pJ/m and a saturation magnetization of 1060 kA/m submitted to a transverse applied magnetic field $\mu_0 H_0 = 30$ mT, as obtained with our plane-wave normal-mode analysis code [26]. The gray circles indicate mode anticrossings. (b)–(d) Same as in (a) for Co-Fe-B/Py bilayers with (b) $l_{\text{Co-Fe-B}} = l_{\text{Py}} = 19$ nm, (c) $l_{\text{Co-Fe-B}} = l_{\text{Py}} = 17$ nm, and (d) $l_{\text{Co-Fe-B}} = l_{\text{Py}} = 25$ nm. The gray ellipses highlight regions where the group velocity of MSSW mode 0 is small. All dispersion relations shown are calculated with the SWIIM numerical method.

each other and hybridize, as revealed by the appearance of mode anticrossings in their dispersion [see Fig. 1(a), which shows the dispersion relation calculated with the SWIIM numerical method]. This hybridization plays a crucial role in obtaining plateaus in the dispersion, which are characteristic of spin waves with vanishing group velocity. For a magnetically symmetric film, the hybridization effect is similar for both positive and negative values of the in-plane wave vector k [Fig. 1(a)]. In a bilayer film made of two magnetic materials with different saturation magnetization M_S , in contrast, mode coupling is nonreciprocal [Fig. 1(b)]: For one sign of k (positive here), modes repel each other (much) more strongly than for the other sign (see Ref. [28]). This asymmetry leads quite systematically to the existence of a rather wide k range where the first MSSW mode is only weakly dispersive and group velocity is low [gray shaded regions in Figs. 1(b)–1(d)], while it remains large for counterpropagating waves with the same frequency. For large thicknesses, mode repulsion can even lead to surface waves exhibiting an unusual backward character (phase velocity $v_p = \omega/k$ and group velocity $v_g = \partial\omega/\partial k$ with opposite signs); see the arrow in Fig. 1(d). A similar backward inflection associated with

the existence of a nonreciprocal magnetostatic interface mode [29,30] was also predicted for magnetic bilayers in the hypothetical pure-dipolar regime [31].

The nonreciprocal flattening of the dispersion relation of MSSW modes in bilayers is quite generic. *A priori*, it can be obtained with use of any two magnetic materials with sufficiently different M_S values [32]. Once these are chosen, designing an optimal diode device amounts to adjusting the composition of the bilayer (total thickness l and/or individual thicknesses of the two layers l_j , with $j = 1, 2$) so as to obtain a frequency plateau as flat as possible [Figs. 1(b)–1(d)]. Numerical simulations show that this can usually be achieved in many ways (not shown). With the ferromagnetic alloys chosen for the present study, namely, $\text{Co}_{40}\text{Fe}_{40}\text{B}_{20}$ (abbreviated as Co-Fe-B) [$M_{S,\text{Co-Fe-B}} = 1270$ kA/m, $A_{\text{Co-Fe-B}} = 17$ pJ/m] and permalloy (Py) ($M_{S,\text{Py}} = 845$ kA/m, $A_{\text{Py}} = 12.8$ pJ/m), $l_{\text{Co-Fe-B}} = l_{\text{Py}} = 19$ nm is a good choice [Fig. 1(b)]. In Sec. III, we use a different composition of the bilayer, namely, $l_{\text{Co-Fe-B}} = 20$ nm and $l_{\text{Py}} = 26$ nm, which yields a slightly broader plateau.

B. Theoretical model

To describe the peculiar magnetization dynamics in a bilayer film and to account for the occurrence of nonreciprocal mode hybridization, we may resort to the theory of dipole-exchange spin waves [33] and use a similar analytical approach as previously developed to account for frequency nonreciprocities of surface waves induced by asymmetric surface anisotropies [21]. Here, for simplicity, we make two strong assumptions: (i) first, we take $l_1 = l_2$, which allows us to decompose the profile of the saturation magnetization through the film thickness $M_S(x)$ into the sum of a mean $\langle M_S \rangle = (M_{S,1} + M_{S,2})/2$ and an antisymmetric deviation $\langle M_S \rangle a(x)$, where $a(x) = \beta \text{sgn} x$ and $\beta = (M_{S,1} - M_{S,2})/(M_{S,1} + M_{S,2})$ denotes the contrast of saturation magnetization between the two materials; (ii) second, we assume that the ratio of the exchange constant to the saturation magnetization has a constant value $A_1/M_{S,1} = A_2/M_{S,2} = \langle A \rangle / \langle M_S \rangle$ throughout the film. In these conditions, the linearized Landau-Lifshitz equation for plane spin waves of the form $\mathbf{m}(x, z, t) = M_S(x) \mathbf{n}(x, z, t) = M_S(x) \boldsymbol{\eta}(x) e^{i(\omega t - kz)}$ can be written as

$$\begin{aligned} i\omega \boldsymbol{\eta}(x) &= -\gamma \mu_0 H_0 \boldsymbol{\eta}(x) \times \hat{\mathbf{y}} \\ &+ \gamma \frac{2\langle A \rangle}{\langle M_S \rangle} \left(\frac{\partial^2}{\partial x^2} - k^2 \right) \boldsymbol{\eta}(x) \times \hat{\mathbf{y}} \\ &+ \gamma \mu_0 \langle M_S \rangle \int_{-l/2}^{l/2} \bar{\bar{G}}_k(x - x') [1 + a(x')] \\ &\times (\boldsymbol{\eta}(x') \times \hat{\mathbf{y}}) dx', \end{aligned} \quad (1)$$

where γ is the gyromagnetic ratio [34], μ_0 is the vacuum permeability, $\hat{\mathbf{y}}$ is a unit vector along the applied magnetic

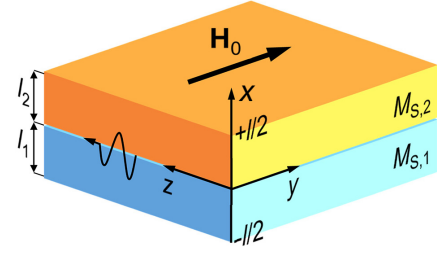


FIG. 2. The bilayer system considered in the analytical model in Sec. II B.

field \mathbf{H}_0 [Fig. 2], and $\bar{\bar{G}}_k$ is the magnetostatic Green's function. Using as a vector basis the x and z components of the first two unpinned exchange modes with homogeneous ($n = 0$) and fully antisymmetric ($n = 1$) profiles of the magnetization precession angle across the film thickness [35], that is, the four-vector set $\{S_0 \hat{\mathbf{x}}, S_0 \hat{\mathbf{z}}, S_1 \hat{\mathbf{x}}, S_1 \hat{\mathbf{z}}\}$ with $S_0(x) = 1/\sqrt{l}$ and $S_1(x) = \sqrt{2/l} \sin(\pi x/l)$, we can rewrite Eq. (1) in the form of an eigenvalue equation $i\Omega \bar{\eta} = \bar{\bar{C}} \bar{\eta}$, where $\Omega = \omega/(\gamma \mu_0 \langle M_S \rangle)$ is a dimensionless frequency, $\bar{\eta} = (\eta_{0,x}, \eta_{0,z}, \eta_{1,x}, \eta_{1,z})^T$, and $\bar{\bar{C}}$ is a dynamic matrix [21].

As an opportunity to introduce useful notation, we first discuss the case of a single layer with exchange constant $\langle A \rangle$ and saturation magnetization $\langle M_S \rangle$ ($\beta = 0$). For such an “unperturbed” system, $\bar{\bar{C}}$ is written as

$$\bar{\bar{C}} = \begin{pmatrix} \bar{\bar{C}}_{00} & \bar{\bar{C}}_{01} \\ \bar{\bar{C}}_{10} & \bar{\bar{C}}_{11} \end{pmatrix} = \begin{pmatrix} 0 & \Omega_{0,z} & -iQ & 0 \\ -\Omega_{0,x} & 0 & 0 & iQ \\ iQ & 0 & 0 & \Omega_{1,z} \\ 0 & -iQ & -\Omega_{1,x} & 0 \end{pmatrix}, \quad (2)$$

with

$$\begin{aligned} \Omega_{0,x} &= 1 - P_{00} + h + \Lambda^2 k^2, \\ \Omega_{0,z} &= P_{00} + h + \Lambda^2 k^2, \\ \Omega_{1,x} &= 1 - P_{11} + h + \Lambda^2 k^2 + \frac{\Lambda^2 \pi^2}{l^2}, \\ \Omega_{1,z} &= P_{11} + h + \Lambda^2 k^2 + \frac{\Lambda^2 \pi^2}{l^2}, \end{aligned} \quad (3)$$

where $1 - P_{00} = (1 - e^{-|k|l})/(|k|l)$, P_{00} , $1 - P_{11}$, and $P_{11} = k^2 l^2 / (\pi^2 + k^2 l^2) \{1 - [2k^2 l^2 / (\pi^2 + k^2 l^2)] [(1 + e^{-|k|l}) / (|k|l)]\}$ are k -dependent self-demagnetizing factors for the $S_0 \hat{\mathbf{x}}$, $S_0 \hat{\mathbf{z}}$, $S_1 \hat{\mathbf{x}}$, and $S_1 \hat{\mathbf{z}}$ basis components, respectively, $h = H_0 / \langle M_S \rangle$ is a dimensionless applied magnetic field, and $\Lambda^2 = 2\langle A \rangle / (\mu_0 \langle M_S \rangle^2)$. The coupling between the uniform and antisymmetric sets of basis functions is described through the off-diagonal $\bar{\bar{C}}_{01} = \bar{\bar{C}}_{10}^*$ blocks, which involve the nonreciprocal mutual-demagnetizing factor $Q = \sqrt{2}kl/(\pi^2 + k^2 l^2)(1 + e^{-|k|l})$.

Solving for $\det(\bar{C} - i\Omega\bar{1}) = 0$, where $\bar{1}$ is the identity matrix, we obtain the eigenfrequencies of the first two hybrid MSSW modes in a single layer:

$$\Omega_{0,1}^2 = \frac{\Omega_{00}^2 + \Omega_{11}^2}{2} - Q^2 \mp \frac{1}{2} \sqrt{(\Omega_{11}^2 - \Omega_{00}^2)^2 + 4Q^2 \left[(P_{00} - P_{11})^2 - \frac{\Lambda^4 \pi^4}{l^4} \right]}, \quad (4)$$

where $\Omega_{nm} = \sqrt{\Omega_{n,x}\Omega_{n,z}}$ ($n = 0, 1$) are the dimensionless frequencies of the uncoupled uniform and antisymmetric precession modes, $\bar{\eta}_0 = (\eta_{0,x}, \eta_{0,z}, 0, 0)^T$ and $\bar{\eta}_1 = (0, 0, \eta_{1,x}, \eta_{1,z})^T$, respectively. Noticeably, the frequencies of the hybrid modes, Ω_0 and Ω_1 , depend on Q^2 , meaning that, although Q obeys $Q(-k) = -Q(k)$, hybridization does not effectively produce nonreciprocity [Fig. 1(a)]. The basic reason for this is that hybridization implies an action of mode $\bar{\eta}_m$ on mode $\bar{\eta}_n$ (e.g., under the influence of mode $\bar{\eta}_1$, mode $\bar{\eta}_0$ acquires an antisymmetric component) as well as a back-action of mode $\bar{\eta}_n$ on mode $\bar{\eta}_m$, both of which are proportional to the coupling factor Q .

With these considerations in mind, we are now ready to consider the case of a magnetic bilayer. When $\beta \neq 0$, the diagonal elements in the \bar{C}_{nn} blocks and the off-diagonal elements in the $\bar{C}_{n \neq m}$ blocks are no longer zero and the dynamic matrix becomes (see Appendix A)

$$\bar{C}(\beta) = \bar{C}(0) + \begin{pmatrix} -iP'_{00} & 0 & 0 & Q' \\ 0 & iP'_{00} & Q' - I' & 0 \\ 0 & Q' & -iP'_{11} & 0 \\ Q' - I' & 0 & 0 & iP'_{11} \end{pmatrix}, \quad (5)$$

where $\bar{C}(0)$ is given by Eq. (2) and

$$\begin{aligned} P'_{00} &= \frac{1}{kl} \left[\sinh(|k|l) - 2 \sinh\left(\frac{|k|l}{2}\right) \right] \beta, \\ P'_{11} &= \frac{2kl}{(\pi^2 + k^2 l^2)^2} (\pi - |k|l e^{-|k|l/2})^2 \beta, \\ I' &= \frac{2\sqrt{2}}{\pi} \beta, \\ Q' &= \frac{2\sqrt{2}}{\pi^2 + k^2 l^2} \left[\pi (1 - e^{-|k|l/2}) + k^2 l^2 \left(\frac{1}{\pi} - \frac{1 - e^{-|k|l}}{2|k|l} \right) \right] \beta. \end{aligned} \quad (6)$$

Not surprisingly, all newly nonzero matrix elements are proportional to the contrast in saturation magnetization β . The coefficients P'_{nn} describe the additional self-demagnetizing effects produced by the magnetic asymmetry on uncoupled modes $\bar{\eta}_n$ ($n = 0, 1$). As revealed by the

imaginary character of the corresponding matrix elements in the \bar{C}_{nn} blocks, these take the form of transverse dipole fields, which oscillate with a phase difference of $\pi/2$ with respect to the dynamic magnetization components creating them. The coefficients Q' and I' , on the other hand, account for the additional mutual-demagnetizing effects produced in the presence of magnetic asymmetry. They describe how hybridization between the uniform and fully antisymmetric modes is affected in a bilayer. The coefficient I' , in particular, corresponds to the local part of the dipole interaction, that is, the usual perpendicular-to-plane demagnetizing effect (see Appendix A). It does not depend on k and plays a similar role as a difference in magnetic anisotropies in the top and bottom parts of the film [21]. Therefore, by analogy, we expect it to be responsible for frequency nonreciprocity.

Solving for $\det[\bar{C}(\beta) - i\Omega\bar{1}] = 0$ and keeping only terms up to first order in β , we obtain the following dispersion relation for the two lowest-frequency MSSW modes in a bilayer [36]:

$$\begin{aligned} (\Omega_0^2 - \Omega^2)(\Omega_1^2 - \Omega^2) - 2Q\Omega [(Q' - I')(\Omega_{1,z} - \Omega_{0,z}) + Q'(\Omega_{1,x} - \Omega_{0,x})] &= 0. \end{aligned} \quad (7)$$

Treating further QQ' and QI' as small parameters, in a perturbative manner, we can obtain the eigenfrequencies of these modes as

$$\Omega_{0,1}(\beta) = \Omega_{0,1}(0) \pm \Delta\Omega(\beta), \quad (8)$$

where $\Omega_0(0)$ and $\Omega_1(0)$ are given by Eq. (4) and

$$\begin{aligned} \Delta\Omega(\beta) &= \frac{Q}{\Omega_1^2(0) - \Omega_0^2(0)} [(I' - Q')(\Omega_{1,z} - \Omega_{0,z}) - Q'(\Omega_{1,x} - \Omega_{0,x})]. \end{aligned} \quad (9)$$

The expression for $\Delta\Omega$ involves two products of dipolar matrix elements, QQ' and QI' . In both of them, one term (Q' or I') is even in k and the other (Q) is odd. Then $\Delta\Omega$ is odd in k and, since $\Omega_0(0)$ and $\Omega_1(0)$ are fully reciprocal, $|\Delta\Omega|$ is a measure of the frequency nonreciprocities for the two hybrid MSSW modes. Noticeably, the nonreciprocities of these hybrid modes have the same magnitude but opposite signs. In both QQ' and QI' products, also, one term (Q' or I') connects the same components (either x or z) for the two uncoupled modes $\bar{\eta}_n$ ($n = 0, 1$), while the other term (Q) connects two different components (x and z). These peculiar combinations allow indirect chiral couplings (of dipolar origin) to develop between the two components of each mode $\bar{\eta}_n$ through hybridization with mode $\bar{\eta}_{m \neq n}$. In Figs. 3(a)–3(c), we illustrate this crucial point in the simplest case of the $\bar{\eta}_0$ mode and of the QI'

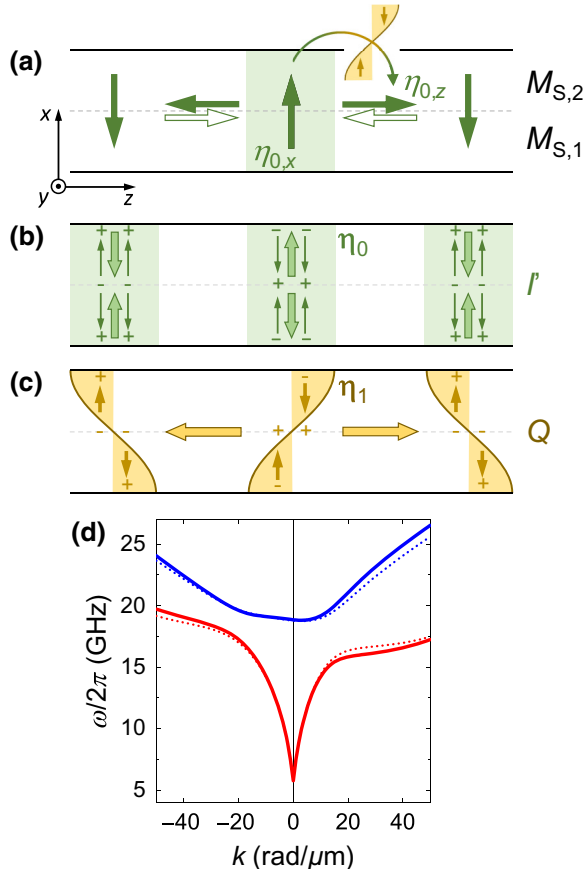


FIG. 3. (a) Indirect QI' coupling between the in-plane and out-of-plane components of uniform mode $\bar{\eta}_0$ through hybridization with antisymmetric mode $\bar{\eta}_1$. Schematic representation of $\bar{\eta}_0$ for positive k (solid arrows) and negative k (open arrows). (b) Illustration of the I' coupling ($\beta > 0$). For a bilayer, the homogeneous precession angle in $\bar{\eta}_0$ translates into an asymmetric distribution of dynamic magnetization. The out-of-plane component of its antisymmetric part (thin green arrows) generates additional magnetic charges and, in turn, an antisymmetric dipole field (thick green arrows), which couples to the out-of-plane component of $\bar{\eta}_1$. (c) Illustration of the Q coupling. The out-of-plane component of $\bar{\eta}_1$ (thin yellow arrows) produces a symmetric in-plane dipole field (thick yellow arrows), which couples to the in-plane component of $\bar{\eta}_0$ in opposite ways depending on the sign of k [compare the relative orientation of the thick horizontal arrows in (a),(c)]. (d) Dispersion relations of the two lowest-frequency MSSW modes in a bilayer with $l_1 + l_2 = 34$ nm, $\langle M_S \rangle = 1000$ kA/m, $\langle A \rangle = 15$ pJ/m, and $\beta = 0.1$. Predictions of the analytical model [Eqs. (8) and 9] and results of numerical simulations are shown as solid and dotted lines, respectively.

product, which plays by far the most-important role among the two products, as one may easily verify numerically. Figure 3(d) compares predictions of the analytical model described above [Eqs. (8) and (9)] with results from numerical simulations in the case of a bilayer with $l_1 + l_2 = 34$ nm, $\langle M_S \rangle = 1000$ kA/m, $\langle A \rangle = 15$ pJ/m, and $\beta = 0.1$. Rather good agreement is observed, which confirms the

essential role played by the QQ' and QI' chiral couplings identified through the analytical modeling in producing nonreciprocal mode repulsion. We note that these chiral couplings bear some resemblance to those at play in the unidirectional emission of spin waves by nanoscale magnetic transducers [14,37]. Here, however, they are not introduced through transduction (excitation/detection) but they are an intrinsic property of the medium, which supports spin-wave propagation.

III. EXPERIMENTAL RESULTS

A. Sample fabrication

The bilayer films used in the present work are deposited on natively oxidized intrinsic Si(100) substrates by dc magnetron sputtering from material targets with nominal compositions of $\text{Co}_{40}\text{Fe}_{40}\text{B}_{20}$ and $\text{Ni}_{80}\text{Fe}_{20}$. Deposition of the magnetic stack is preceded by that of a 3-nm-thick Ta seed layer to ensure low layer roughness and is followed by that of a 3-nm-thick Au overlayer to protect the magnetic alloys against oxidation. For propagating-spin-wave-spectroscopy and microfocused-Brillouin-light-scattering experiments, devices are fabricated out of these films by means of standard clean-room processes, involving laser and electron-beam lithographies, as well as ion milling [20,38]. These consist of 10- μm -wide magnonic waveguides covered with a 120-nm-thick insulating layer of silicon oxide and two pairs of emitting and receiving microwave antennas made from a Ti(10 nm)/Al(90 nm) stack placed above (see Sec. III C).

B. Nonreciprocal dispersion relations

The dispersion relations of thermally excited spin waves in the $\text{Co}_{40}\text{Fe}_{40}\text{B}_{20}$ (20 nm)/ $\text{Ni}_{80}\text{Fe}_{20}$ (26 nm) bilayer system are determined by wave-vector-resolved-Brillouin-light-scattering experiments [39,40] performed on a plain film. To evidence the nonreciprocal character of these dispersions, both Stokes and anti-Stokes peaks are recorded for the two possible polarities of the applied magnetic field in the MSSW configuration ($\mathbf{H}_0 \perp \mathbf{k}$).

Figures 4(a)–4(c) shows BLS spectra obtained with $\mu_0 H_0 = +30$ mT at different values of the in-plane wave vector k . Four different peaks, two Stokes and two anti-Stokes peaks, can be identified, which are related to the first (red) and second (blue) MSSW branches. These peaks are fitted to Lorentzian lines to extract their central frequencies and thereby reconstruct the $f(k)$ curves. The dispersion relations obtained are found to be in very good agreement with theoretical predictions [Fig. 4(d)]. As required to fulfill our ambition to build a magnonic diode, a well-defined frequency plateau is present at about 12.5 GHz in the dispersion of MSSW mode 0, which corresponds to the anti-Stokes peak with k -independent position

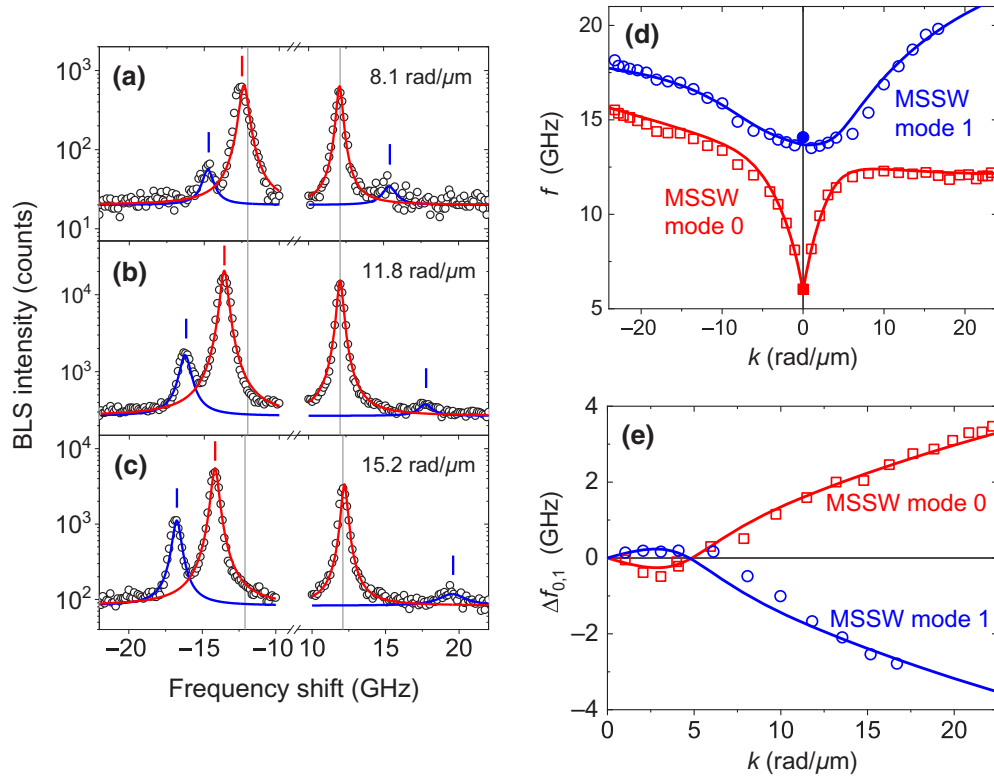


FIG. 4. (a)–(c) BLS spectra recorded in the DE configuration ($\mu_0 H_0 = 30$ mT) on a $\text{Co}_{40}\text{Fe}_{40}\text{B}_{20}$ (20 nm)/ $\text{Ni}_{80}\text{Fe}_{20}$ (26 nm) bilayer film (symbols) for three different values of the in-plane wave vector: (a) $|k| = 8.1$ rad/ μm , (b) $|k| = 11.8$ rad/ μm , and (c) $|k| = 15.2$ rad/ μm . Lines are guides for the eye. (d) Dispersion relations of the two lowest-frequency MSSW modes deduced from BLS data (open symbols) and comparison with predictions from numerical simulations (lines). Solid symbols correspond to data from a complementary ferromagnetic resonance experiment. (e) Frequency nonreciprocities $\Delta f_n(k) = f_n(-|k|) - f_n(+|k|)$ of MSSW modes 0 and 1. As in (d), symbols and lines correspond to experimental and numerical data, respectively.

in Figs. 4(a)–4(c). Clear experimental evidence is then provided for the occurrence of nonreciprocal slow spin waves in our system.

The anti-Stokes peak with highest frequency has a small amplitude whatever the value of k [Figs. 4(a)–4(c)]. The peak even becomes undetectable for wave-vector values exceeding 17 rad/ μm ; hence the lack of some (blue) data points in Figs. 4(d) and 4(e). This is attributed to the fact that, as verified in numerical simulations (see Appendix B), MSSW mode 1 has a very small amplitude in the uppermost part of the bilayer film, whose magneto-optic contribution dominates the BLS signal. The frequency nonreciprocities of the two MSSW modes, $\Delta f_n(k) = f_n(-|k|) - f_n(+|k|)$ ($n = 0, 1$), show very specific behaviors [Fig. 4(e)]. First, $\Delta f_0(k)$ and $\Delta f_1(k)$ are almost equal in absolute value and opposite in sign, which comes naturally in our analytical theory of the nonreciprocal hybridization (Sec. II B). Second, these quantities do not vary monotonously as a function of k . Instead, they exhibit a local extremum followed by a change of sign at about 5 rad/ μm .

Following the same line of thought as used to explain the nonintuitive localization of dipole-exchange MSSW

modes [17,20], this change of sign can be ascribed to a transition between a regime dominated by exchange across the film thickness, in the $k \rightarrow 0$ limit, to a regime where in-plane dipole fields gain importance, at larger k . On hybridization, indeed, out-of-plane exchange interactions and dipole interactions produce additional torques that compete with each other and give terms with opposite signs in the expression for $\Delta\Omega$ [Eq. (9)]. To better see this, we may expand the elements of the dynamic matrix \bar{C} [Eqs. (3) and (6)] in a Taylor series around $kl = 0$. Keeping only terms up to second order in kl , we obtain

$$\Delta\Omega(\beta) = \frac{8kl}{\pi^3[\Omega_1^2(0) - \Omega_0^2(0)]} \times \left[\frac{\Lambda^2\pi^2}{l^2} - \frac{|k|l}{2} \left(1 + 3\frac{\Lambda^2\pi^2}{l^2} \right) \right] \beta, \quad (10)$$

where we identify the first term between the square brackets (i.e., $\Lambda^2\pi^2/l^2$) as being of pure exchange origin and the second one as being proportional to the k -dependent self-demagnetizing factor $P_{00}(k) \simeq |k|l/2$, as arising from dipole-dipole interactions. According to this expression, a

change of sign of $\Delta\Omega$ is expected at the particular value $|k^*| = \{(l/2)[3 + l^2/(\Lambda\pi)^2]\}^{-1}$, which indeed amounts to a few radians per micrometer for magnetic materials with $\Lambda \simeq 4$ nm and thickness l in the 40–50-nm range. Such a change of sign has also been predicted for films where breaking of the top-bottom magnetic symmetry is not obtained through a blockwise variation of M_S , like here, but rather by a grading of saturation magnetization across the thickness [22]. In contrast, it has not been observed for bilayers where the two magnetic materials, being separated by a nonmagnetic spacer, are coupled only through long-range dipole interactions [41,42]. This further demonstrates the essential role played by short-range out-of-plane exchange coupling in this phenomenon.

C. Magnonic diode behavior

1. Propagating-spin-wave spectroscopy

To clearly demonstrate the diodelike behavior of the bilayer system studied, PSWS experiments are performed on specially designed devices [Fig. 5(a)], each one containing a pair of 50- μm -long, 10- μm -wide bilayer waveguides and two pairs of single-wire antennas connected in parallel. A typical PSWS experiment is performed in the following way: a vector network analyzer is connected to the antennas to serve both as a generator and as a detector for determining the complex mutual inductance L_{ij} of the two antennas pairs. On injection of a current with adequate frequency f in the emitting antennas (index j), these couple inductively to the magnetization of the waveguides and spin waves are excited. If those waves travel far enough and reach the receiving antennas (index i) before being fully damped, a microwave magnetic flux with frequency f is picked up. The ratio of the measured flux to the injected current defines the mutual inductance L_{ij} of interest [38,43]. In practice, to extract spin-wave-related signals more accurately, relative measurements are systematically taken, wherein a background signal, which is acquired at much-larger applied magnetic field so that no spin-wave resonance occurs, is subtracted from the raw data. The device layout chosen [Fig. 5(a)], in which spin waves are traveling simultaneously along two magnetic buses, ensures a good symmetry match with the ground-signal-ground microwave probes used for connection to the vector network analyzer. Importantly, the 200-nm-wide single-wire antennas used here can couple inductively to spin waves with a broad range of wave vectors, $0 \leq |k| \leq k_{\text{max}}$, where $k_{\text{max}} \simeq 12$ rad/ μm . The distance between the emitting and receiving antennas ($D = 2$ μm or 5 μm) is adapted to the typical attenuation length expected for surface spin waves with such k values in a $\text{Co}_{40}\text{Fe}_{40}\text{B}_{20}$ (20 nm)/ $\text{Ni}_{80}\text{Fe}_{20}$ (26 nm) bilayer.

Figure 5(b) shows the real part of the spin-wave-induced change in mutual inductance ΔL_{ij} as a function of frequency for a device with a relatively large distance

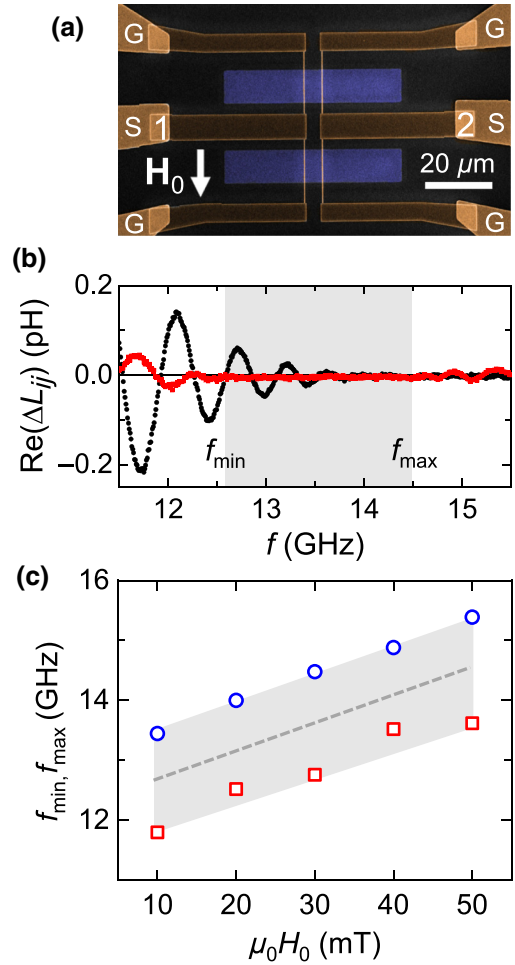


FIG. 5. Propagating-spin-wave spectroscopy. (a) False-color scanning electron micrograph of a PSWS device with distance $D = 5$ μm between the emitting and receiving antennas. G, ground; S, signal. (b) Real part of the spin-wave-induced change in mutual inductance ΔL_{ij} as a function of the excitation frequency f ($\mu_0 H_0 = 30$ mT), for spin waves propagating from antennas 1 to antennas 2 ($k > 0$, red squares) and vice versa ($k < 0$, black circles) in the device in (a). (c) Upper limit (f_{max} , blue circles) and lower limit (f_{min} , red squares) of the frequency gap for rightward-propagating spin waves as a function of the applied magnetic field, as deduced from PSWS data such as shown in (b).

between the emitting and receiving antennas [$D = 5$ μm , see Fig. 5(a)] submitted to a transverse in-plane magnetic field $\mu_0 H_0 = +30$ mT. The two data sets presented correspond to opposite directions of spin-wave propagation. Comparing them, one immediately sees that the spin-wave signal at 12.5 GHz $\leq f \leq 14.5$ GHz is vanishingly small for $k > 0$ (red symbols), meaning that no spin waves travel from the left antennas to the right antennas, whereas it is comparatively large for $k < 0$ (black symbols) as spin waves do propagate effectively from the right antennas to the left antennas. This nonreciprocal behavior is, of course, related to the presence of a plateau in the positive- k part of

the dispersion relation of MSSW mode 0 [Fig. 4(d)], which has two main consequences. First, rightward-propagating spin waves with $f \simeq 12.5$ GHz and $0 \leq k \leq k_{\max}$ are excited by the left antennas but, due to their very low group velocity, they die out under the effect of magnetic damping before reaching the receiving antennas. Second, because of the large extension of the plateau, the group velocity of MSSW mode 0 becomes sizable again only for k values that lie far beyond the k range accessible with the antennas used, meaning that rightward-propagating MSSW-mode-0 spin waves with frequency well above 12.5 GHz are simply not produced. For $f \geq 14.5$ GHz, MSSW mode 1 eventually gets excited, and so a clear spin-wave signal is transmitted again for both directions of propagation. An effective forbidden gap with a width of about 2 GHz is thus formed for rightward-propagating spin waves [shaded zone in Fig. 5(b)]. In view of the possible application of this phenomenon, it is worth mentioning that the gap can naturally be shifted up and down in frequency by adjustment of the amplitude of the applied magnetic field. Tunability on the order of 50 MHz/mT is measured experimentally over the 10–50-mT range [Fig. 5(c)].

Because the wave vector k is constrained to change according to the dispersion relation $k(f)$, the phase delay kD acquired by spin waves after propagation over the distance D varies continuously as the frequency f is swept. This variation in phase delay translates into pronounced oscillations of the recorded spin-wave signal [Fig. 5(b)]. As we describe below, this provides us with a way to extract the wave-vector value corresponding to each driving frequency f . For that, one needs to record both the real part and the imaginary part of the spin-wave-induced change in mutual inductance over a large range of frequencies [Fig. 6(a,c)] encompassing the ferromagnetic resonance frequency (FMR), $f_{\text{FMR}} = f_0(k=0)$, which corresponds to the onset of the oscillations [44]. From such data, the spin-wave wave vector can be determined as

$$k(f) = \pm \frac{\phi_{ij}(f) - \phi_0}{D}. \quad (11)$$

In this expression, the \pm sign accounts for the change of sign of k on reversal of the direction of spin-wave propagation [$+$ corresponding to spin waves traveling from the left antennas ($j=1$) to the right ones ($i=2$)], $\phi_0 = \pi/2$ is the reference phase at f_{FMR} , where ΔL_{ij} is purely imaginary (pure absorption), and, more importantly, $\phi_{ij}(f) = \arg[\Delta L_{ij}(f)] + 2n\pi$ (with n an integer) is the spin-wave phase, which must be unwrapped in a continuous manner, starting from f_{FMR} .

The open symbols in Fig. 6(b) show the dispersion relation of MSSW mode 0 reconstructed by applying the method described above [Eq. (11)] to ΔL_{ij} data recorded between 5.8 and 14.5 GHz [45]. As expected, for $k > 0$, the dispersion can be followed up to only approximately

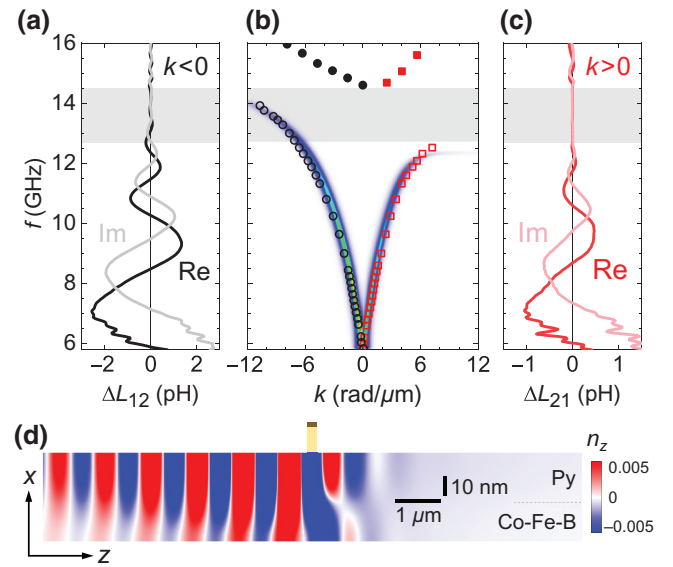


FIG. 6. Spin-wave propagation in a device with $D = 2 \mu\text{m}$. (a),(c) Real and imaginary parts of ΔL_{ij} as a function of frequency for $k < 0$ (a) and $k > 0$ (c). (b) Dispersion relations of the lowest (open symbols) and second-lowest (solid symbols) MSSW branches deduced from the experimental spin-wave signals shown in (a),(c), and spin-wave spectral weight (color map) as obtained from mumax³ micromagnetic simulations. See the text for details. (d) Simulated cross-section map of the in-plane component of the normalized dynamic magnetization, $n_z = m_z/M_S$, for an excitation frequency of 12.5 GHz. The lateral extension of the single-wire antenna is indicated by the horizontal brown bar and the insulating layer of silicon oxide is sketched as a yellow layer (not to scale vertically). The alternating current assumed in the antenna is 3 mA, which yields an in-plane magnetic field of about 3 mT at the top surface of the bilayer, directly beneath the source.

+7 rad/ μm , which corresponds to the lower edge of the frequency plateau. In contrast, for $k < 0$, it can be followed down to -12 rad/ μm , thus confirming the ability of our PSWS device to probe the expected wave-vector range $[-k_{\max}, +k_{\max}]$. As support for our conclusions, Fig. 6(b) also displays in the background the “weighted” dispersion relation computed for a Co-Fe-B(20 nm)/Py(26 nm) bilayer with the mumax³ using space and time Fourier transforms of in-plane magnetization traces obtained under square-pulse excitation of 10-ps duration. The simulations, which use elementary cell sizes $h_x = 0.5$ nm, $h_y = 10$ nm, and $h_z = 4$ nm and periodic boundary conditions in the longitudinal (z) and transverse (y) in-plane directions [46], include a realistic spatial distribution for the excitation field produced by the antenna and account for magnetic losses through Gilbert damping factors of 0.008 and 0.012 for Co-Fe-B and Py, respectively (see Sec. 2). Very good agreement between the two kinds of data may be observed, particularly regarding the asymmetric way in which the amplitude of the transmitted spin-wave vanishes as f is

increased. Figure 6(d) shows a cross-section map of the dynamic magnetization as generated under continuous-wave excitation at $f = 12.5$ GHz, which illustrates how this nonreciprocity translates in real space: once the excitation frequency enters the gap, the dynamic magnetization profile becomes essentially evanescent on the right side of the source as the far-field coupling of the antenna to the magnetic precession vanishes. Noticeably, micromagnetic simulations reveal a similar behavior in the “overshoot” regime, where the dispersion of MSSW mode 0 contains a region with backward character [Fig. 1(d)]: the lower-frequency limit of the gap then corresponds to the local maximum in the $\omega(k)$ curve of MSSW mode 0.

2. Microfocused Brillouin light scattering

To visualize directly the spatial decay of spin waves, we perform microfocussed-BLS imaging [40] on a similar device as used for PSWS [Fig. 5(a)]. In those experiments, the spin-wave intensity is mapped next to an antenna while microwave power (-5 dBm) is continuously injected into it. In the DE configuration, switching the direction of the

equilibrium magnetization is equivalent to reversing the wave vector \mathbf{k} [20,47]. Then, instead of looking at both sides of the source to image counterpropagating waves, we concentrate on one side and record spin-wave intensity maps for the two polarities of the transversally applied magnetic field. Accordingly, the data obtained for $H_0 < 0$ are mirrored horizontally in Figs. 7(a) and 7(c). The benefit of this experimental strategy is that it allows us to probe counterpropagating spin waves in the very same optical conditions, thus avoiding artifacts related, for instance, to differences in the surface state of the waveguide.

To support these observations, mumax³ simulations are also performed for a finite, $50\text{-}\mu\text{m}$ -long, $10\text{-}\mu\text{m}$ -wide bilayer strip. The expected BLS signal is calculated by assuming that it is mostly related to the out-of-plane component of the dynamic magnetization (m_x) at the top surface of the magnetic medium. As in the experiments, spin waves are excited by an alternating magnetic field with frequency f produced by a 100-nm -thick, 200-nm -wide antenna located 120 nm above the spin-wave conduit. For each magnetic cell (with size $h_x = 4$ nm, $h_y = 40$ nm, and $h_z = 8$ nm [48]), the time dependence of m_x is recorded

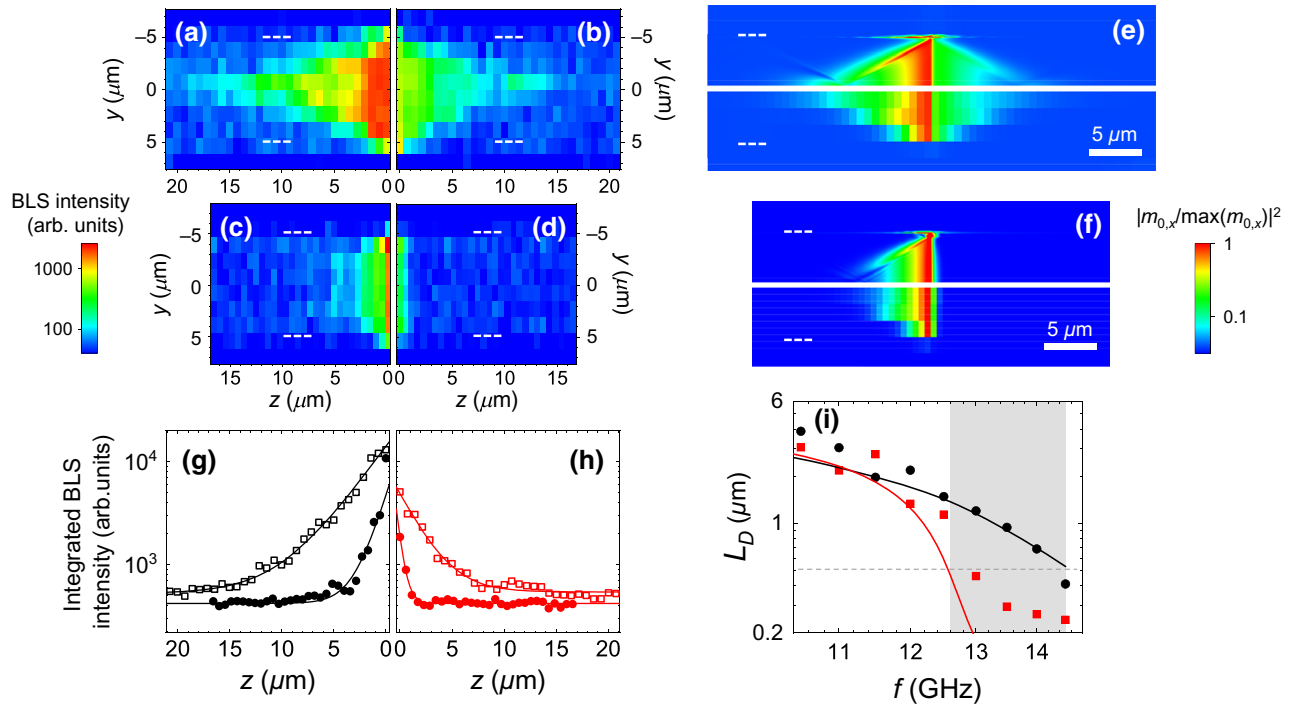


FIG. 7. (a)–(d) Experimental BLS-intensity maps for excitation frequencies of 11 GHz (a),(b) and 13 GHz (c),(d) and applied magnetic fields $\mu_0 H_0 = -30$ mT (a),(c) and $\mu_0 H_0 = +30$ mT (b),(d) (logarithmic scale). The dashed lines indicate the position of the waveguide edges. (e),(f) Computed BLS-intensity maps for $f = 11$ GHz (e) and $f = 13$ GHz (f), $\mu_0 H_0 = 30$ mT. The current assumed in the antenna is 0.1 mA (linear regime). In each panel, the upper part shows raw data, whereas the lower part shows pixelated data obtained by averaging raw data over $1.6 \times 0.8 \mu\text{m}^2$ rectangular areas. See the text for further details. (g),(h) z profiles of the BLS intensity integrated over the width of the waveguide as deduced from the maps in (a)–(d). Open and solid symbols correspond to $f = 11$ GHz and $f = 13$ GHz, respectively. The lines are fits of the experimental data to the expression $I(z) = I_0 \exp(-z/L_D) + I_{\text{noise}}$. (i) Variation of the decay length of the spin-wave intensity, L_D , with the excitation frequency f for spin waves propagating to the right ($H_0 > 0$, red) and to the left ($H_0 < 0$, black). The symbols and the solid lines are data derived from experiments and simulations, respectively. The horizontal dashed line indicates the smallest spin-wave wavelength compatible with the antenna design chosen.

over a full period $1/f$ in the steady excitation regime and analyzed to extract its maximum value $m_{0,x}$. Finally, normalized intensity maps are constructed, which show $|m_{0,x}/\max(m_{0,x})|^2$, either with the full resolution of the simulations [top panels in Figs. 7(e) and 7(f)] or with a degraded resolution mimicking that of microfocused-BLS images [bottom panels in Figs. 7(e) and 7(f)]. Overall, good agreement is obtained between experimental and computed images, assuming damping values of 0.008 and 0.012 for Co-Fe-B and Py, respectively [49]. Quite naturally, on pixelation, sharp features, such as those related to localized edge modes, tend to be washed out. However, for $f = 11$ GHz, long oblique contrast arising from the interference between the fundamental and higher-order width modes of the waveguide remains discernible [Figs. 7(a) and 7(e)].

As expected, for frequencies in the range 6–12 GHz (i.e., below the frequency plateau), significant spin-wave intensity is systematically detected up to distances of several micrometers from the antenna [Figs. 7(a), 7(b), and 7(e)]. Although plateau-related spin-wave filtering is not yet active, a difference in intensity may be observed between the two directions of propagation. This is nothing but the usual amplitude nonreciprocity of magnetostatic surface waves, which follows from the fact that a transducer placed on one side of a waveguide couples differently to counterpropagating surface waves [50]. When the frequency reaches 13 GHz (above the frequency plateau), on the other hand, the spin-wave intensity remains relatively large for one direction of propagation [Figs. 7(c) and 7(f)] but drops abruptly for the opposite one [Figs. 7(d) and 7(f)]. On the basis of the discussion above, we naturally attribute this fast drop in intensity to the phenomenon of spin-wave slowdown associated with the presence of a plateau in the positive- k part of the dispersion relation of MSSW mode 0.

This phenomenon is best illustrated by extracting the spin-wave decay length L_D from the BLS data. For this, one may simply average the spin-wave intensity over the width of the waveguide (i.e., along y) so as to mitigate finite-width effects [51], plot the integrated intensity as a function of the space coordinate along the direction of propagation, z , and fit this dependence to an exponential decay of the form $I(z) = I_0 \exp(-z/L_D) + I_{\text{noise}}$ [see Figs. 7(g) and 7(h)]. Figure 7(i) shows the variation of L_D with f obtained by treating the experimental data and the numerical data in this manner. A clear difference in behavior may be observed depending on the sign of k . For spin waves traveling to the left ($k < 0$, black circles and black line), L_D decreases steadily with increasing f . For spin waves traveling to the right ($k > 0$, red squares and red line), in contrast, this steady decay is interrupted by a sudden drop in L_D as f reaches the frequency of the plateau, f_p . Beyond f_p , L_D becomes smaller than the minimum spin-wave wavelength $2\pi/k_{\text{max}} \simeq 0.5 \mu\text{m}$ attainable with our single-wire antenna. This reveals the evanescent

character of the magnetization dynamics induced when the frequency falls into the effective gap, also evidenced in the micromagnetic simulation in Fig. 6(d).

IV. CONCLUSION

In the present work, the concept of a spin-wave diode is proposed that makes use of the particular dynamic dipolar interactions in transversally magnetized media. The device is made from a thin film consisting of two exchange-coupled layers with different saturation magnetizations. Our theoretical analysis reveals that, in such a film, chiral dipolar couplings develop, which results in nonreciprocal hybridization between close-lying spin-wave branches. Using this phenomenon, we engineer carefully the dispersion of surface waves so as to reduce the group velocity of waves traveling in a particular direction to a very low value (slow waves), while maintaining a large value for those propagating the other way. A comprehensive experimental picture of the diode functioning is obtained by combining propagating-spin-wave spectroscopy with Brillouin light scattering in both reciprocal-space thermal mode and real-space imaging mode: the magnetization dynamics excited by a source of finite size take the form of genuinely propagating waves in the forward direction of the diode and reduce to evanescent waves in the reverse one. By design, our spin-wave diode is quite versatile as its operational frequency window can be adjusted by tuning the amplitude of the applied magnetic field and its forward and reverse directions can be interchanged by switching the polarity of the field. Since our concept of spin-wave diode relies on fully-built-in rather than transduction-related nonreciprocity, it could contribute decisively to the advance toward the all-magnon approach for computing [9]. As a concluding remark, we point out that engineering of unidirectionally slow spin waves could also prove useful in more-general situations where long interaction times are needed within a limited space; for instance, for promoting nonreciprocal nonlinear coupling in the channel of a magnonic transistor [52].

ACKNOWLEDGMENTS

This work was funded by the French National Research Agency (ANR) through the Programme d'Investissement d'Avenir under contract ANR-11-LABX-0058_NIE within the Programme d'Investissement d'Avenir ANR-10-IDEX-0002-02. The authors acknowledge the STnano clean-room facility for technical support and the High Performance Computing center of the University of Strasbourg for access to computing resources, part of which were funded by the EquipEx Equip@Meso project of the Programme Investissements d'Avenir. M. Geilen and P.P. acknowledge funding by Deutsche Forschungsgemeinschaft Grant No. TRR 173-268565370 (project B01).

M.G. and M.G. contributed equally to this work. Y.H. and D.S. performed the micromagnetic simulations. M.B. and D.L. developed the analytical model. M.H. grew the films. M.G. and D.L. fabricated the devices and performed the inductive measurements. M.G. performed the BLS experiments. M.B., P.P., and Y.H. supervised the project. Y.H., M.G., M.G., M.B., and P.P. wrote the manuscript. All authors discussed the results.

APPENDIX A: ADDITIONAL DYNAMIC MATRIX ELEMENTS FOR A BILAYER FILM

We derive analytical expressions for the additional elements that appear in the dynamic matrix for magnetostatic surface waves on top-bottom disymmetrization of the magnetic film through blockwise variations of the saturation magnetization and exchange constant (see Sec. II B). In the linearized Landau-Lifshitz equation [Eq. (1)], the perturbation thus introduced is described by the term

$$\gamma \mu_0 \langle M_S \rangle \int_{-l/2}^{l/2} \bar{\bar{G}}_k(x-x') a(x') [\boldsymbol{\eta}(x') \times \hat{\mathbf{y}}] dx'. \quad (\text{A1})$$

Therefore, the corrections to be added to the $\bar{\bar{C}}$ matrix are four 2×2 blocks, each of which has the form

$$\bar{\bar{A}}_{nm} = \begin{pmatrix} -A_{nm}^{zx} & -A_{nm}^{zz} \\ A_{nm}^{xx} & A_{nm}^{zz} \end{pmatrix}, \quad (\text{A2})$$

with

$$A_{nm}^{ij} = \int_{-l/2}^{l/2} dx \int_{-l/2}^{l/2} dx' S_n(x) G_k^{ij}(x-x') a(x') S_m(x'). \quad (\text{A3})$$

Here indices $n, m = 0, 1$ refer to the uniform and anti-symmetric basis functions introduced in Sec. II B and the G_k^{ij} 's ($i, j = x, z$) are the four components of the tensorial magnetostatic Green's function, which read [33]

$$\begin{aligned} G_k^{zz}(s) &= -\frac{|k|}{2} e^{-|ks|}, \\ G_k^{xx}(s) &= -\delta(s) - G_k^{zz}(s), \\ G_k^{xz}(s) &= G_k^{zx}(s) = -i \operatorname{sgn}(ks) G_k^{zz}(s), \end{aligned} \quad (\text{A4})$$

where $\delta(s)$ is Dirac's δ function. Since the functions $a(x)$, $G_k^{xz}(s)$, $G_k^{zx}(s)$, and $S_1(x)$ are odd and $G_k^{xx}(s)$, $G_k^{zz}(s)$, and $S_0(x)$ are even, half of these matrix elements are strictly nil: $A_{nn}^{ii} = A_{n \neq m}^{i \neq j} = 0$. Moreover, from Eqs. (A3) and (A4), it is easy to see that one necessarily has $A_{nm}^{ij} = A_{nm}^{ji}$. Then, overall, only four independent quantities must be calculated: A_{00}^{xz} , A_{11}^{xz} , A_{01}^{xx} , and A_{01}^{zz} .

We start with A_{00}^{xz} and A_{11}^{xz} , which both involve G_k^{xz} . According to Eqs. (A3) and (A4), A_{00}^{xz} can be written as

$$\begin{aligned} A_{00}^{xz} &= \int_{-l/2}^{l/2} dx \int_{-l/2}^{l/2} dx' S_0(x) G_k^{xz}(x-x') a(x') S_0(x') \\ &= i \frac{\beta |k|}{2l} \int_{-l/2}^{l/2} dx \int_{-l/2}^{l/2} dx' \operatorname{sgn}[k(x-x')] e^{-|k(x-x')|} \operatorname{sgn} x'. \end{aligned} \quad (\text{A5})$$

After some long but straightforward algebra for dealing with the absolute value and sign functions, we obtain

$$A_{00}^{xz} = iP'_{00} = i \frac{\beta}{kl} [\sinh(|k|l) - 2 \sinh(|k|l/2)]. \quad (\text{A6})$$

Similarly, for A_{11}^{xz} , we have

$$\begin{aligned} A_{11}^{xz} &= \int_{-l/2}^{l/2} dx \int_{-l/2}^{l/2} dx' S_1(x) G_k^{xz}(x-x') a(x') S_1(x') \\ &= i \frac{\beta |k|}{l} \int_{-l/2}^{l/2} dx \sin\left(\frac{\pi x}{l}\right) \\ &\quad \times \int_{-l/2}^{l/2} dx' \operatorname{sgn}[k(x-x')] e^{-|k(x-x')|} \operatorname{sgn} x' \sin\left(\frac{\pi x'}{l}\right), \end{aligned} \quad (\text{A7})$$

from which we obtain

$$A_{11}^{xz} = iP'_{11} = i \frac{2\beta kl}{\pi^2 + k^2 l^2} (\pi - |k|l e^{-|k|l/2}). \quad (\text{A8})$$

As made explicit in Eq. (A4), the xx component of the tensorial Green's function is composed of two terms, a local term (δ function) corresponding to the usual, k -independent out-of-plane demagnetizing field and a non-local, k -dependent correction involving G_k^{zz} . Accordingly, the matrix element A_{01}^{xx} may be decomposed as

$$A_{01}^{xx} = -I' + Q', \quad (\text{A9})$$

with

$$\begin{aligned} I' &= \int_{-l/2}^{l/2} dx \int_{-l/2}^{l/2} dx' S_0(x) \delta(x-x') a(x') S_1(x') \\ &= \frac{\beta \sqrt{2}}{l} \int_{-l/2}^{l/2} dx \int_{-l/2}^{l/2} dx' \delta(x-x') \operatorname{sgn} x' \sin\left(\frac{\pi x'}{l}\right) \end{aligned} \quad (\text{A10})$$

and

$$\begin{aligned} Q' &= \int_{-l/2}^{l/2} dx \int_{-l/2}^{l/2} dx' S_0(x) G_k^{zz}(x-x') a(x') S_1(x') \\ &= \frac{\beta |k|}{\sqrt{2}l} \int_{-l/2}^{l/2} dx \int_{-l/2}^{l/2} dx' e^{-|k(x-x')|} \operatorname{sgn} x' \sin\left(\frac{\pi x'}{l}\right). \end{aligned} \quad (\text{A11})$$

As before, the double integrations in Eqs. (A10) and (A11) require only basic algebra and we obtain

$$I' = \frac{2\sqrt{2}\beta}{\pi} \quad \text{and}$$

$$Q' = \frac{2\sqrt{2}\beta}{\pi^2 + k^2 l^2} \times \left[\pi (1 - e^{-|k|l/2}) + k^2 l^2 \left(\frac{1}{\pi} - \frac{1 - e^{-|k|l}}{2|k|l} \right) \right]. \quad (\text{A12})$$

Finally, for A_{01}^{zz} , we simply have

$$A_{01}^{zz} = \int_{-l/2}^{l/2} dx \int_{-l/2}^{l/2} dx' S_0(x) G_k^{zz}(x-x') a(x') S_1(x') = Q'. \quad (\text{A13})$$

APPENDIX B: SPIN-WAVE MODAL PROFILES

We present examples of spin-wave eigenmodes [Fig. 8] obtained as solutions for a Co-Fe-B(20 nm)/Py(26 nm) bilayer using the SWIIM numerical method [26]. The magnetic parameters are the same as those used to calculate the dispersion relation in Fig. 4(d) and the modal profiles discussed here are those for $|k| = 20$ rad/ μm . We start by considering only $|\eta|$; that is, the norm of the variable magnetization normalized to M_S [Figs. 8(a) and 8(b)]. Two important conclusions can be drawn from these data.

(a) First, the mode with lowest frequency, MSSW mode 0, has maximum amplitude at the top surface for both directions of propagation [see the red lines in Figs. 8(a) and 8(b)]. This is different from the behavior of MSSW modes in thicker films ($l > 100$ nm), where leftward-propagating and rightward-propagating spin waves are confined near opposite surfaces [17]. This clearly shows that one cannot relate directly the frequency nonreciprocity that we observe to a preferential localization of counterpropagating spin waves in the two different materials that constitute the bilayer.

(b) Second, for $k > 0$, the second-lowest-frequency mode, MSSW mode 1, always has a small amplitude near the top surface of the film. This amplitude reaches virtually zero for $k \simeq +20$ rad/ μm [see the blue line in Fig. 8(a)]. This explains why the anti-Stokes peak corresponding to MSSW mode 1 is globally much weaker than its Stokes counterpart [Figs. 4(a)–4(c)] and why, as mentioned in Sec. III A, it becomes hardly discernible for k in the range 17–25 rad/ μm .

If instead of looking at mode amplitudes, we now consider the in-plane (η_z) and out-of-plane (η_x) components of the variable magnetization separately, as is done in [Fig. 8(c)] for MSSW mode 0 with $k < 0$, the hybrid character of this mode appears very clearly: the modal profile

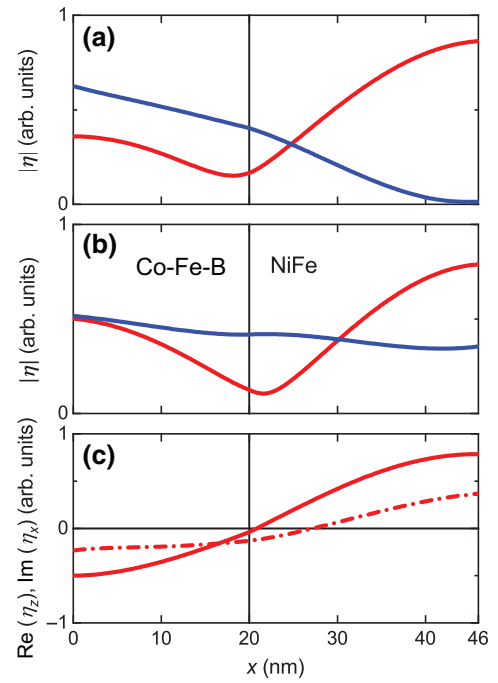


FIG. 8. Depth profiles of MSSW mode 0 and MSSW mode 1 in the Co-Fe-B(20 nm)/Py(26 nm) bilayer stack as computed with the SWIIM numerical method ($\mu_0 H_0 = +30$ mT). (a),(b) Amplitude of the dynamic magnetization normalized to M_S versus vertical coordinate x for $k = +20$ rad/ μm (a) and $k = -20$ rad/ μm (b). Red lines (blue lines) correspond to MSSW mode 0 (MSSW mode 1). (c) In-plane (solid line) and out-of-plane (dash-dotted line) components of the reduced dynamic magnetization in MSSW mode 0 as a function of the vertical coordinate x for $k = -20$ rad/ μm .

contains both a uniform (S_0 -like) contribution and an anti-symmetric (S_1 -like) contribution. Noticeably, the relative weights of these contributions are not the same for the two components, which translates into nodes located at different depths for η_x and η_z . This justifies the need for using a set of four vectors (as opposed to a set of only two vectors) as a basis for the dynamic matrix model developed in Sec. II B.

- [1] D. Jalas, A. Petrov, M. Eich, W. Freude, S. Fan, Z. Yu, R. Baets, M. Popović, A. Melloni, J. D. Joannopoulos, M. Vanwolleghem, C. R. Doerr, and H. Renner, What is and what is not an optical isolator, *Nat. Photon.* **7**, 579 (2013).
- [2] L. D. Landau and E. M. Lifshitz, *Electrodynamics of Continuous Media* (Pergamon Press, Oxford, 1960).
- [3] H. Lira, Z. Yu, S. Fan, and M. Lipson, Electrically Driven Nonreciprocity Induced by Interband Photonic Transition on a Silicon Chip, *Phys. Rev. Lett.* **109**, 033901 (2012).
- [4] N. Reiskarimian and H. Krishnaswamy, Magnetic-free non-reciprocity based on staggered commutation, *Nat. Commun.* **7**, 11217 (2016).

- [5] A. C. Mahoney, J. I. Colless, S. J. Pauka, J. M. Hornibrook, J. D. Watson, G. C. Gardner, M. J. Manfra, A. C. Doherty, and D. J. Reilly, On-Chip Microwave Quantum Hall Circulator, *Phys. Rev. X* **7**, 011007 (2017).
- [6] S. A. H. Gangaraj and F. Monticone, Topological Waveguiding near an Exceptional Point: Defect-Immune, Slow-Light, and Loss-Immune Propagation, *Phys. Rev. Lett.* **121**, 093901 (2018).
- [7] C. E. Fay and R. L. Comstock, Operation of the ferrite junction circulator, *IEEE Trans. Microwave Theory Tech.* **13**, 15 (1965).
- [8] A. Khitun and K. L. Wang, Non-volatile magnonic logic circuits engineering, *J. Appl. Phys.* **110**, 034306 (2011).
- [9] A. V. Chumak, in *Spintronics Handbook - Spin-Transport and Magnetism*, edited by E. Y. Tsymlal and I. Žutić (CRC Press, Boca Raton, 2019), Vol. 1, Chap. 6, p. xxx.
- [10] T. Fischer, M. Kewenig, D. A. Bozhko, A. A. Serga, I. I. Syvorotka, F. Ciubotaru, C. Adelmann, B. Hillebrands, and A. V. Chumak, Experimental prototype of a spin-wave majority gate, *Appl. Phys. Lett.* **110**, 152401 (2017).
- [11] Q. Wang, R. Verba, T. Brächer, P. Pirro, and A. Chumak, Integrated magnonic half-adder, arXiv:1902.02855.
- [12] J. Lan, W. Yu, R. Wu, and J. Xiao, Spin-Wave Diode, *Phys. Rev. X* **5**, 041049 (2015).
- [13] T. Brächer, O. Boulle, G. Gaudin, and P. Pirro, Creation of unidirectional spin-wave emitters by utilizing interfacial Dzyaloshinskii-Moriya interaction, *Phys. Rev. B* **95**, 064429 (2017).
- [14] J. Chen, T. Yu, C. Liu, T. Liu, M. Madami, K. Shen, J. Zhang, S. Tu, M. Shah Alam, K. Xia, M. Wu, G. Gubbiotti, Y. M. Blanter, G. E. W. Bauer, and H. Yu, Excitation of unidirectional exchange spin waves by a nanoscale magnetic grating, *Phys. Rev. B* **100**, 104427 (2019).
- [15] F. López-Tejiera, S. G. Rodrigo, L. Martín-Moreno, F. J. García-Vidal, E. Devaux, T. W. Ebbesen, J. R. Krenn, I. P. Radko, S. I. Bozhevolnyi, M. U. González, J. C. Weeber, and A. Dereux, Efficient unidirectional nanoslit couplers for surface plasmons, *Nat. Phys.* **3**, 324 (2007).
- [16] R. W. Damon and J. R. Eshbach, Magnetostatic modes of a ferromagnet slab, *J. Phys. Chem. Solids* **19**, 308 (1961).
- [17] M. Kostylev, Non-reciprocity of dipole-exchange spin waves in thin ferromagnetic films, *J. Appl. Phys.* **113**, 053907 (2013).
- [18] B. Hillebrands, Spin-wave calculations for multilayered structures, *Phys. Rev. B* **41**, 530 (1990).
- [19] P. Khalili Amiri, B. Rejaei, M. Vroubel, and Y. Zhuang, Nonreciprocal spin wave spectroscopy of thin Ni/Fe stripes, *Appl. Phys. Lett.* **91**, 062502 (2007).
- [20] M. Haidar, M. Bailleul, M. P. Kostylev, and Y. Lao, Non-reciprocal Oersted field contribution to the current-induced frequency shift of magnetostatic surface waves, *Phys. Rev. B* **89**, 094426 (2014).
- [21] O. Gladii, M. Haidar, Y. Henry, M. Kostylev, and M. Bailleul, Frequency nonreciprocity of surface spin wave in permalloy thin films, *Phys. Rev. B* **93**, 054430 (2016).
- [22] R. A. Gallardo, P. Alvarado-Seguel, T. Schneider, C. Gonzalez-Fuentes, A. Roldán-Molina, K. Lenz, J. Lindner, and P. Landeros, Spinwave non-reciprocity in magnetization-graded ferromagnetic films, *New J. Phys.* **21**, 033026 (2019).
- [23] S. R. Seshadri, Surface magnetostatic modes on a ferrite slab, *Proc. IEEE* **58**, 506 (1970).
- [24] S. Shichi, N. Kanazawa, K. Matsuda, S. Okajima, T. Hasegawa, T. Okada, T. Goto, H. Takagi, and M. Inoue, Spin wave isolator based on frequency displacement non-reciprocity in ferromagnetic bilayer, *J. Appl. Phys.* **117**, 17D125 (2015).
- [25] M. Bailleul, D. Olligs, and C. Fermon, Propagating spin wave spectroscopy in a permalloy film: A quantitative analysis, *Appl. Phys. Lett.* **83**, 972 (2003).
- [26] Y. Henry, O. Gladii, and M. Bailleul, Propagating spin-wave normal modes: A dynamic matrix approach using plane-wave demagnetizing tensors, arXiv:1611.06153.
- [27] A. Vansteenkiste, J. Leliaert, M. Dvornik, M. Helsen, F. Garcia-Sanchez, and B. Van Waeyenberge, The design and verification of MuMax3, *AIP Adv.* **4**, 107133 (2014).
- [28] K. Kalinikos and P. A. Kolodin, Excitation of propagating spin waves in multilayered ferromagnetic film structures, *J. Magn. Magn. Mater.* **83**, 103 (1990).
- [29] T. Wolfram, Magnetostatic surface waves in layered magnetic structures, *J. Appl. Phys.* **41**, 4748 (1970).
- [30] R. E. Camley and A. A. Maradudin, Magnetostatic interface waves in ferromagnets, *Solid State Comm.* **41**, 585 (1982).
- [31] G. Rupp, W. Wetling, and W. Jantz, Surface spin waves in anisotropic magnetic multilayers, *Appl. Phys. A* **42**, 45 (1987).
- [32] Similar behavior can be observed for magnetic films containing a smooth gradient of M_S throughout the thickness; see Ref. [22]. These are, however, much more difficult to fabricate experimentally and to model analytically.
- [33] B. A. Kalinikos and A. N. Slavin, Theory of dipole-exchange spin wave spectrum for ferromagnetic films with mixed exchange boundary conditions, *J. Phys. C* **19**, 7013 (1986).
- [34] Throughout this entire paper, we assume $\gamma/2\pi = 29.2$ GHz/T, which is the value determined from ferromagnetic resonance experiments performed on single layers of $\text{Co}_40\text{Fe}_{40}\text{B}_{20}$ and permalloy.
- [35] Exchange modes are defined here as eigenmodes of the exchange operator; see Ref. [33].
- [36] $P_n n'$ coefficients appear in this relation only at second order in β .
- [37] Y. Au, E. Ahmad, O. Dmytriiev, M. Dvornik, T. Davison, and V. V. Kruglyak, Resonant microwave-to-spin-wave transducer, *Appl. Phys. Lett.* **100**, 182404 (2012).
- [38] V. Vlaminck and M. Bailleul, Spin-wave transduction at the submicrometer scale: Experiment and modeling, *Phys. Rev. B* **81**, 014425 (2010).
- [39] P. Grünberg, in *Light Scattering in Solids V. Topics in Applied Physics*, edited by M. Cardona and G. Güntherodt (Springer, Berlin, Heidelberg, 1989), Vol. 66/1, Chap. 8, p. 303.
- [40] T. Sebastian, K. Schultheiss, B. Obry, B. Hillebrands, and H. Schultheiss, Micro-focused Brillouin light scattering: Imaging spin waves at the nanoscale, *Front. Phys.* **3**, 35 (2015).
- [41] M. Mruczkiewicz, P. Graczyk, P. Lupo, A. Adeyeye, G. Gubbiotti, and M. Krawczyk, Spin-wave nonreciprocity and magnonic band structure in a thin permalloy film

- induced by dynamical coupling with an array of Ni stripes, [Phys. Rev. B **96**, 104411 \(2017\)](#).
- [42] R. A. Gallardo, T. Schneider, A. K. Chaurasiya, A. Oelschlägel, S. S. .P. K. Arekapudi, A. Roldán-Molina, R. Hübner, K. Lenz, A. Barman, J. Fassbender, J. Lindner, O. Hellwig, and P. Landeros, Reconfigurable Spin-Wave Non-Reciprocity Induced by Dipolar Interaction in a Coupled Ferromagnetic Bilayer, [Phys. Rev. Appl. **12**, 034012 \(2019\)](#).
- [43] V. Vlaminck and M. Bailleul, Current-induced spin-wave doppler shift, [Science **322**, 410 \(2008\)](#).
- [44] The short-period small-amplitude oscillations of the mutual inductance observed at frequencies between 6 and 7 GHz are related to reflections of the spin waves at the extremities of the magnetic waveguides.
- [45] When applied to ΔL_{ij} data taken above 14.5 GHz, Eq. (11) also allows determining the dispersion relation of MSSW mode 1, see solid symbols in Fig. 6(b).
- [46] To mimic the behavior of an extended film, a $46\text{nm} \times 10\text{nm} \times 131072\text{nm}$ unit cell is used, which is repeated, respectively, 2048 and 16 times along the y and z directions.
- [47] R. Camley, Nonreciprocal surface waves, [Surf. Sci. Rep. **7**, 103 \(1987\)](#).
- [48] Here the cell size in the transverse (y) direction is larger than the exchange length. However, tests performed using cells 10 times smaller allowed us to check that this does not affect the obtained static configuration.
- [49] These values are significantly larger than those determined for Co-Fe-B (0.004) and Py (0.006) from usual FMR experiments performed on as-deposited single layers of those materials. Yet, these are the values that must be assumed to reach a good agreement when trying to reproduce, in numerical simulations, the spatial decay of spin waves observed experimentally through microfocused Brillouin Light Scattering. Such an increase in damping could be related to the nanofabrication process.
- [50] T. Schneider, A. A. Serga, T. Neumann, B. Hillebrands, and M. P. Kostylev, Phase reciprocity of spin-wave excitation by a microstrip antenna, [Phys. Rev. B **77**, 214411 \(2008\)](#).
- [51] Interferences between width modes of the waveguide with even symmetries, in particular the fundamental mode ($n = 0$) and the third width mode ($n = 2$), are washed out when averaging the spin-wave intensity over the width of the magnetic strip, so that the decay length extracted here are not influenced by such effects.
- [52] A. V. Chumak, A. A. Serga, and B. Hillebrands, Magnon transistor for all-magnon data processing, [Nat. Commun. **5**, 4700 \(2014\)](#).